

Atomic delocalization as a microscopic origin of two-level defects in Josephson junctions

This content has been downloaded from IOPscience. Please scroll down to see the full text.

2015 *New J. Phys.* 17 023017

(<http://iopscience.iop.org/1367-2630/17/2/023017>)

View the [table of contents for this issue](#), or go to the [journal homepage](#) for more

Download details:

IP Address: 115.64.111.83

This content was downloaded on 05/02/2015 at 12:11

Please note that [terms and conditions apply](#).

New Journal of Physics

The open access journal at the forefront of physics

Deutsche Physikalische Gesellschaft 

IOP Institute of Physics

Published in partnership
with: Deutsche Physikalische
Gesellschaft and the Institute
of Physics



PAPER

OPEN ACCESS

RECEIVED
12 September 2014

REVISED
19 November 2014

ACCEPTED FOR PUBLICATION
31 December 2014

PUBLISHED
4 February 2015

Atomic delocalization as a microscopic origin of two-level defects in Josephson junctions

Timothy C DuBois, Salvy P Russo and Jared H Cole

Chemical and Quantum Physics, School of Applied Sciences, RMIT University, Melbourne, 3001, Australia

E-mail: timothy.dubois@rmit.edu.au

Keywords: two level defects, Josephson junction, phase qubit

Content from this work
may be used under the
terms of the [Creative
Commons Attribution 3.0
licence](#).

Any further distribution of
this work must maintain
attribution to the author
(s) and the title of the
work, journal citation and
DOI.



Abstract

Identifying the microscopic origins of decoherence sources prevalent in Josephson junction (JJ) based circuits is central to their use as functional quantum devices. Focussing on so called ‘strongly coupled’ two-level defects, we construct a theoretical model using the atomic position of the oxygen which is spatially delocalized in the oxide forming the JJ barrier. Using this model, we investigate which atomic configurations give rise to two-level behaviour of the type seen in experiments. We compute experimentally observable parameters for phase qubits and examine defect response under the effects of applied electric field and strain.

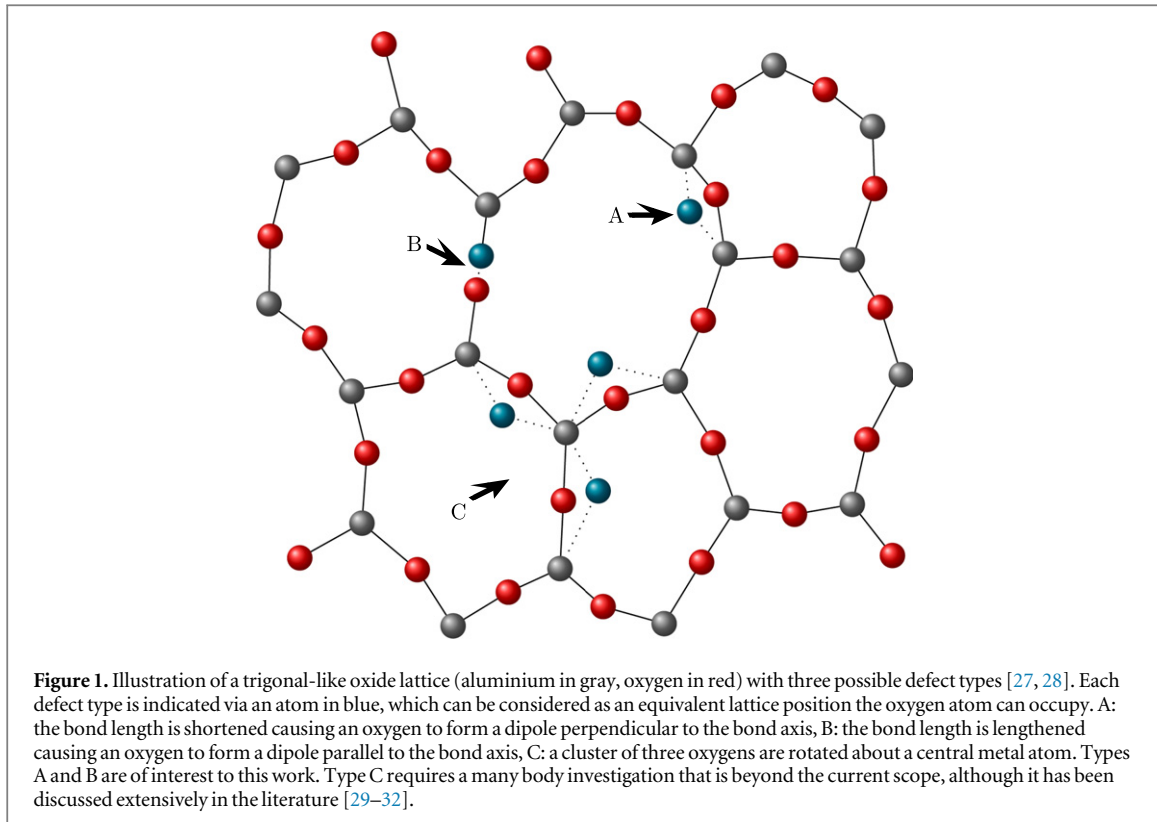
1. Introduction and concept

Superconducting qubits and Josephson junction (JJ) based quantum devices in general are often limited by decoherence sources. A common and important source of decoherence is the environmental two-level system (TLS) [1, 2]. Experiments have probed these defects directly and shown them to be stable, controllable and have relatively long decoherence times [3–8], although little is known about their true microscopic nature. Many phenomenological theories attempting to describe them exist; including charge dipoles [9], Andreev bound states [10], magnetic dipoles [11], Kondo impurities [12] and TLS state dependence of the JJ transparency [13]. Detailed fitting of experimental data can place limits on these models [14] but the scope of free parameters of each model allows them all to fit experimental results—rendering them presently indistinguishable. It is therefore important to construct microscopic models of these systems to increase our understanding of their composition. Polaron dressed electrons [15] and surface aluminium ions paramagnetically coupling to ambient molecules [16] are two recent models that may shed new light in this area.

Bistable defects in glasses and amorphous solids in general have been understood for some time [17]. Amorphous insulating barriers (either in the form of JJs or simply a native oxide) form an integral part of superconducting circuits, so it comes as no surprise that TLSs are often considered to be an important source of noise in these circuits [1, 2, 9]. Developments in controllable qubit architecture (charge, flux and phase) has enabled the study of so-called ‘strongly coupled defects’ [4, 6, 7]. These defects have comparable resonance frequencies to the qubit circuit and coupling strengths as well as decoherence times long enough to allow coherent oscillations between the qubit and TLS. Probing individual defects has promoted their bistable nature from hypothesis to observable fact, as well as providing clues to their microscopic origin.

As described in previous work [18], we consider the origin of some defects to be within the amorphous oxide layer itself, specifically an oxygen atom in a spatially delocalized state. This has important ramifications for materials science based efforts to reduce the effects of TLSs. If, as alternative models suggest, TLS defects indeed stem from surface states [19] or the accidental inclusion of an alien species [20, 21]; future fabrication techniques or more robust qubit designs may suppress or diminish the response of such noise sources as has been the case historically [9, 22–25]. Nevertheless, if the oxygen atoms themselves form a noise source, a perfectly clean but amorphous dielectric may still harbour a large ensemble of TLSs.

Our approach considers only atomic positions as input parameters in an attempt to construct a microscopic model rather than a phenomenological one. The premise of our TLS model is that positional anharmonicity of



oxygen atoms arises within the AlO_x barrier of the JJ primarily due to its non-crystalline nature. As an illustrative example, consider an interstitial oxygen defect in crystalline silicon: the harmonic approximation for atomic positions cannot be applied due to the rotational symmetry of the defect as oxygen delocalizes around the Si–Si bond axis [26]. This forms an anharmonic system with a quasi-degenerate [18] ground state, even in a ‘perfect’ crystal. This ansatz allows the existence of many different spatial configurations throughout the layer, causing unique TLS properties based solely on atomic positions and rotation in relation to the external electric field. To simplify the configuration space we initially consider the introduction of small lattice irregularities from an idealized trigonal-like two-dimension (2D) oxide lattice. Possible defects of this nature are depicted in figure 1.

It has often been suggested that a bath of TLSs are responsible for the weakly coupled, ohmic $1/f$ noise [1]. However, it is unclear if the identified strongly coupled systems are from the same origin. Ultimately many separate microscopic suspects may be identified; although work in this area is not mature enough to speculate. The model in this work therefore only attempts to describe TLSs that are strongly coupled in nature.

The outline of this paper is as follows. Section 2 introduces the theory from which we build our model to investigate delocalized oxygen based TLSs. The following three sections then start from a minimal example of this model and slowly add complexity, so interactions can be examined and understood in a systematic way. Section 3 considers a defect comprising of an Al–O–Al chain in one-dimension (1D), perturbed from a crystalline lattice, simulating defects A and B in figure 1. In reality, an oxygen atom in the amorphous layer of a JJ will be surrounded by atoms in all three dimensions. Moving towards a model representation of this, section 4 extends the model to 2D, with four aluminium atoms confining an oxygen in a plane. The completed model is then described in section 5, which extends oxygen confinement into three dimensions (with six aluminum atoms), whilst still projecting oxygen delocalization on a plane. Although in general an oxygen can delocalize in three dimensions, for this investigation we focus on an effective 2+1 D model, minimizing both computational and descriptive complexity while still modelling the relevant behaviour of the system. The following sections then apply the 2+1 D model and compare delocalized oxygen responses to experimental TLS data. Section 7 discusses qubit–TLS coupling and section 8 observes the effect of mechanical strain.

2. Methods

We are interested in what happens to the oxygen atom as it responds to an external potential exerted via its nearest neighbours, particularly if the bonded aluminium atoms are displaced in a manner similar to the defect types outlined in figure 1. If we also ignore any time evolution properties of the system for now and derive an

effective single particle Hamiltonian

$$H = -\frac{\hbar^2}{2m_{\text{oxy}}} \nabla^2 + V(\mathbf{r}), \quad (1)$$

where m_{oxy} is the mass of an oxygen atom and $V(\mathbf{r})$ is the potential due to the surrounding (mostly amorphous) lattice.

The two most striking properties of a strongly coupled TLS, assuming the charge dipole framework is physically representational, are its ground to first excited state splitting E_{01} and a strong electric dipole moment. Observed values of E_{01} differ between qubit architectures: approximately 1–10 GHz for transmons [23], 4–5 GHz for flux qubits [6] (although recent designs can tune this gap down to the MHz range [33]) and nominally 7–8 GHz for phase qubits [14]. Dipole moment strengths also vary, but are usually on the order of 1 eÅ [5, 14]. Whilst many other properties have been measured, this work will focus on obtaining respectable values for E_{01} and dipole strength, assuming our model defect is embedded inside a fictitious phase qubit. When a representative example is required in this work, $E_{01} = 8$ GHz will be used, to compare directly with TLSs studied in the phase qubits of [14].

A potential which represents the junction, requires a number of capabilities. It needs to describe interactions between atomic species (in this case, Al–Al, O–O and Al–O interactions), as well as many body interactions to be as accurate as possible (which will be required to investigate quasi-degenerate states). As a complete description of many body interactions does not currently exist; potentials of this type tend to be empirically fitted to experimental data in order to obtain physico-chemical properties of a studied system as accurately as possible. The trade off here is that whilst any given potential may describe some properties of the system well because of certain fitting parameters, other properties may be well out of range as they were not included in the study that constructed the potential. Great care was taken to choose the best potential that accurately represented the junction, in this case the empirical Streitz–Mintmire potential [34], which describes a myriad of aluminium oxide properties over quite a large range of temperatures and pressures with high accuracy when compared against similar potentials. It was also chosen over simpler fixed-charge models [35, 36] due to the complex geometry of the JJ. A variable charge potential such as Streitz–Mintmire can capture the variable oxygen states when present in a predominantly metallic environment through the minimization of the electrostatic term in the potential (2). This capability is particularly important here, as our junction has two metal-oxide interfaces, and our TLS defects may reside close to these boundaries.

The Streitz–Mintmire potential is given by

$$V(\mathbf{r}) = E_{\text{EAM}} + \sum_i^N q_i \chi_i + \frac{1}{2} \sum_{i,j}^N q_i q_j V_{ij}, \quad (2)$$

where $q_{\{i,j\}}$ is the atomic charge, $\chi_i = \chi_i^0 + \sum_j Z_j \left(\left[j | f_i \right] - \left[f_i | f_j \right] \right)$ and $V_{ij} = J_i^0 \delta_{ij} + \left[f_i | f_j \right]$. χ_i^0 is the electronegativity and J_i^0 is an empirical parameter known as ‘atomic hardness’ or a self-Coulomb repulsion [37] of atom i . Z_j is an effective core charge of atom j , $\delta_{ij} = 1$ when $i=j$ and $\delta_{ij} = 0$ when $i \neq j$, and all summation is calculated for N atoms of the target system. The square bracket notation represents Coulomb interaction integrals between valence charge densities (e.g. j) and effective core charge densities (e.g. f_i) and takes the form [38]

$$\left[a | f_b \right] = \int \frac{f_b(r_b, q_b)}{r_{av}} dV_b, \quad (3)$$

$$\left[f_a | f_b \right] = \iint \frac{f_a(r_a, q_a) f_b(r_b, q_b)}{r_{vv}} dV_a dV_b \quad (4)$$

with $a = i, j$; $b = i, j$; $a \neq b$ in (2) to prohibit self interactions. $dV_{a,b}$ are integrating volume units. r_{av} is therefore the center distance between atom a and dV_b , and r_{vv} is the center distance between dV_a and dV_b .

The first term in (2), E_{EAM} , does not depend on the partial charges q_i and therefore describes a charge-neutral system, represented here with a quantum mechanical based empirical embedded atom model (EAM) for the Al–Al and Al–O interactions

$$E_{\text{EAM}} = \sum_i^N F_i[\rho_i] + \sum_{i < j}^N \phi_{ij}(r_{ij}), \quad (5)$$

with $F_i[\rho_i]$ as the energy required to embed atom i in a local electron density ρ_i , and $\phi_{ij}(r_{ij})$ describing the residual pair–pair interactions by way of Buckingham and Rydberg potentials

Table 1. Empirical constants for the Streitz–Mintmire pair potentials (6) [34, 39].

| Pair | A | ρ | B | C | r_0 |
|-------|-------------|----------|----------|-----------|----------|
| Al–Al | 4.474755 | 0.991317 | 0.159472 | 5.949144 | 3.365875 |
| Al–O | 62.933909 | 0.443658 | 0.094594 | 9.985407 | 2.358570 |
| O–O | 3322.784218 | 0.291065 | 1.865072 | 16.822405 | 2.005092 |

$$\phi_{ij}(r_{ij}) = A \exp\left(-\frac{r_{ij}}{\rho}\right) - B \left[1 + C \left(\frac{r_{ij}}{r_0} - 1\right)\right] \exp\left[-C \left(\frac{r_{ij}}{r_0} - 1\right)\right], \quad (6)$$

where r_{ij} is the interatomic (Euclidean) distance between atoms i and j , all other constants are listed in table 1. Further formalisms and parameters can be found in [34, 38], implementation is also discussed in [39].

Using this potential, a single body time-independent Hamiltonian is constructed using a 7-point central difference method

$$f''(x_0) = \frac{2f_{-3} - 27f_{-2} + 270f_{-1} - 490f_0 + 270f_1 - 27f_2 + 2f_3}{180h^2} + \mathcal{O}(h^6), \quad (7)$$

where $f_k = f(x_0 + kh)$. The step size $h = 0.1 \text{ \AA}$ was found to be optimal for the grid range relevant to our purposes [40]. A sparse matrix representation of H (1) is then solved via direct diagonalization, obtaining eigenvectors and eigenenergies with precision better than 10 kHz. In contrast, the energy scale for JJ defects observed in experiments is $\lesssim 10 \text{ GHz}$ [4, 6, 7].

The dipole element is computed using numerical integration of the ground- and first-excited states (ψ_0, ψ_1), where

$$\delta\varphi_x = \iint \psi_0^*(x, y) x \psi_1(x, y) dx dy \quad (8)$$

is an example of the dipole in the x direction.

Relative differences in energy levels (i.e. energy splittings) are an important measure of the model. We therefore define a convention where $E_{ij} = E_j - E_i$, such that the ground state (E_0) to first excited state (E_1) energy splitting is defined as E_{01} . For comparison with experimental results, energy is expressed in frequency units throughout this paper.

3. TLS defects as perturbed bond angles in a lattice

Consider the two simplest cases in figure 1—defect type A; where the aluminium–oxygen bond distance is shortened, forcing the oxygen to occupy two off axis positions, and defect type B; where the opposite occurs: aluminium–oxygen bond distance is lengthened, allowing two preferred oxygen positions on axis.

These two defect types can be modelled by solving our system hamiltonian (1) for three atoms: an oxygen with two aluminium atoms at a lattice coordinate apart, displaced toward and away from the oxygen. For example, corundum: the low pressure and temperature phase of aluminium oxide (also known as α -Al₂O₃) has an Al–O bond distance of $\sim 1.85 \text{ \AA}$. If we define the oxygen position to be at an origin, the aluminium atoms can be considered as pairs ($x = -X, +X = \{\pm 1.85 \text{ \AA}\}$) lying on a cardinal axes; which are identified throughout this paper as $|X|$ or simply the ‘defect pair’. Displacing $|X|$ equidistantly from this origin (i.e. moving away from optimal crystalline configuration) will yield either an A or B type defect, depending on the direction of displacement.

An eigenspectrum of the seven lowest energy levels of this system over a continuum of values in $|X|$ is depicted in figure 2. Each energy is measured relative to the ground state, which shows two particular regions where E_{01} (green, solid line) is quasi-degenerate (labelled sections A and B: both associated with the respective defect type). There exists a third (an)harmonic region (section C), which reaches a harmonic state at a separation distance of $|X| \sim 1.85 \text{ \AA}$: the optimal corundum Al–O bond distance. At this distance the spatial harmonic approximation holds and the oxygen can be considered to be localized.

To investigate the potential landscape and the resultant oxygen wavefunction in sections A and B of figure 2, we choose two separation distances: $|X| = 1.5 \text{ \AA}$ (figure 3), which lies in the A type defect section, and $|X| = 2.2 \text{ \AA}$ (figure 4), which exists in the B type defect section. Although the Al–O–Al chain is arranged in a line, we consider delocalization of the oxygen in 2D so that both defect types can be identified on a continuum separation in $|X|$ (as figure 2 depicts) rather than using two separate coordinate systems.

Both figures show a top down view of the potential exerted on the oxygen by the two aluminium atoms (gray), whose positions lie at the centre of the circles. We truncate potential energy values above 0 eV for clarity,

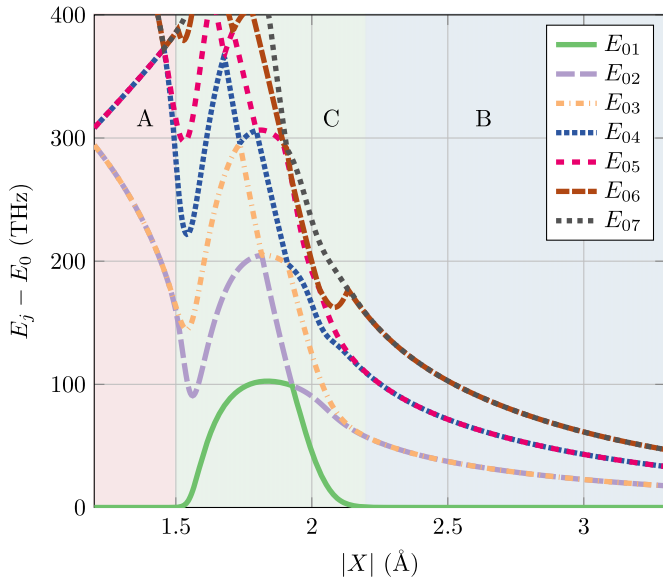


Figure 2. Eigenspectrum of a three atom system Al–O–Al, over a varying distance separation. Each excited state has been normalized with the ground state, which clearly shows two regions with a degeneracy at the lowest level. Section A is indicative of the A type defect (figure 3), section B of the B type (figure 4). An (an)harmonic crossover point is also extant, labelled as section C, which is approximately centered about the optimal Al–O bond distance of corundum (1.85 Å).

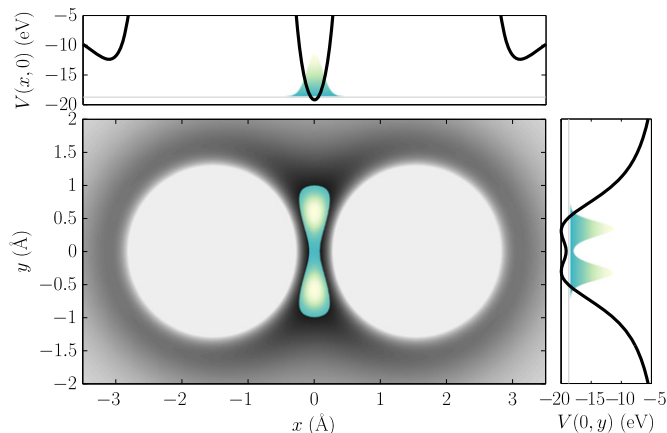


Figure 3. A top down view of the potential seen by an oxygen atom with two aluminium atoms closer than an appropriate lattice distance (truncated at 0 eV, gray). The ground state eigenmode of the oxygen can be seen in the center (green/yellow). This configuration has a separation distance of $|X| = 1.5 \text{ \AA}$ and is representative of an A type defect (see figure 1). 1D potential values and projected wavefunctions, which are anchored to the ground state energy (thin gray line) are plotted in the outsets to better indicate the depth of the potential well.

where energy is measured relative to the zero point set by the Streitz–Mintmire potential’s electronegativity correction. The ground state wavefunction (green/yellow) indicates the spatial probability of the oxygen atom in these configurations. It can be clearly seen in figure 4, where the pair is far apart, two local minima exist in the form of rings around the base of each aluminium position: due to the fact that aluminium oxide is only partially covalent and mostly ionic.

Equivalences between the A and B type defects illustrated in figure 1 are clearly visible: figure 3 showing a shortened bond length, causing an oxygen dipole perpendicular to the bond axis, and figure 4 depicting a lengthened bond and an oxygen dipole parallel to the bond axis.

The functional form of the 1D potential (outset axes of figures 3 and 4, black; either $V(x, 0)$ or $V(0, y)$) in the direction of the defect is a double well. Also depicted in these outsets are projected wavefunctions, which have been scaled for visual purposes, but anchored at the ground state energy (thin gray line). This representation is equivalent to the standard two level physics depiction of the TLS, and as such, potential offsets and tunneling matrix elements of our model may be estimated in this limit.

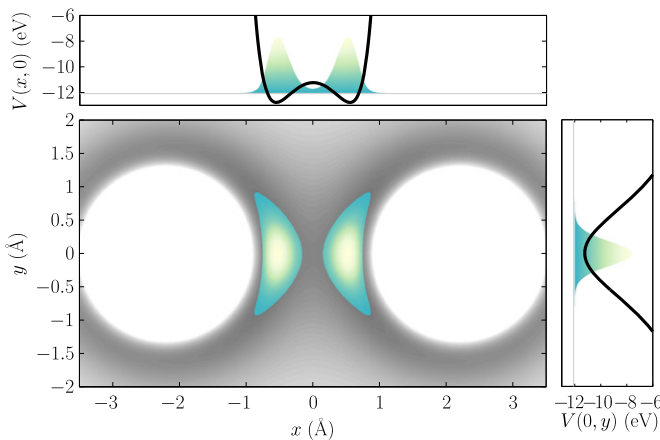


Figure 4. A top down view of the potential seen by an oxygen atom with two aluminium atoms further apart than an appropriate lattice distance (truncated at 0 eV, gray). The ground state eigenmode of the oxygen can be seen in the center (green/yellow). This configuration has a separation distance of $|X| = 2.2 \text{ \AA}$ and is representative of a B type defect (see figure 1). 1D potential values and projected wavefunctions, which are anchored to the ground state energy (thin gray line) are plotted in the outsets to better indicate the depth of the potential well.

4. TLS defect confined in two-dimensions

The ideal case discussed in section 3 ignores many real world complications, in particular any potential constraints from nearest neighbour atoms that undoubtedly surround the TLS. In an attempt to add complexity to the model gradually, we start with two additional aluminium atoms on the same plane as figures 3 and 4, confining the defect in the $|Y|$ direction (i.e. $y = -Y, +Y$).

4.1. Classifying eigenspectrum dynamics

As the values of $|X|$ or $|Y|$ are altered, a complex interplay between the excited states of the model can result. Simple two-level degeneracy and harmonic states are no longer the only possibilities. To interpret what is occurring in a certain domain, we define a metric using the ground and four lowest excited state energies

$$\xi = \frac{E_1 - E_0}{E_2 - E_0} + \frac{E_3 - E_0}{E_4 - E_0}. \quad (9)$$

This metric ranges from 0 to 2 and can give a qualitative understanding of the eigenspectrum of the defect.

To begin we plot a phase space diagram akin to those introduced in [18], where ξ is plotted as a function of the distance to the confining aluminium atoms ($|X|$, $|Y|$). Each phase diagram is split into at least four domains, where the properties of these domains can be explained through the interplay of potential configuration and dipole alignment (discussed in section 6). Focusing for now on the influence of potential shape, the 2D potential can be approximated as two 1D potentials: one projected in the x direction and the other along y . There are two relevant configurations, a set of two double wells (tetra-well) or a set of a double and harmonic well (hemi-tetra-well); which are both illustrated in figure 5. It is clear from the outset potential projections of figures 3 and 4 that both A and B type defects reside in hemi-tetra-wells.

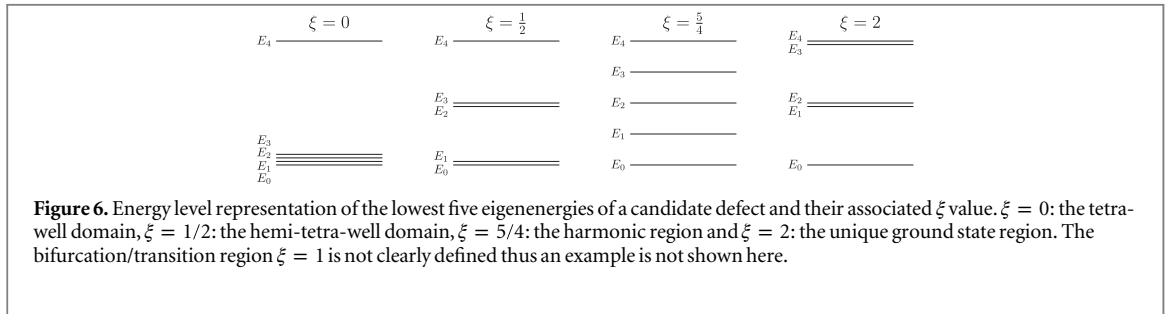
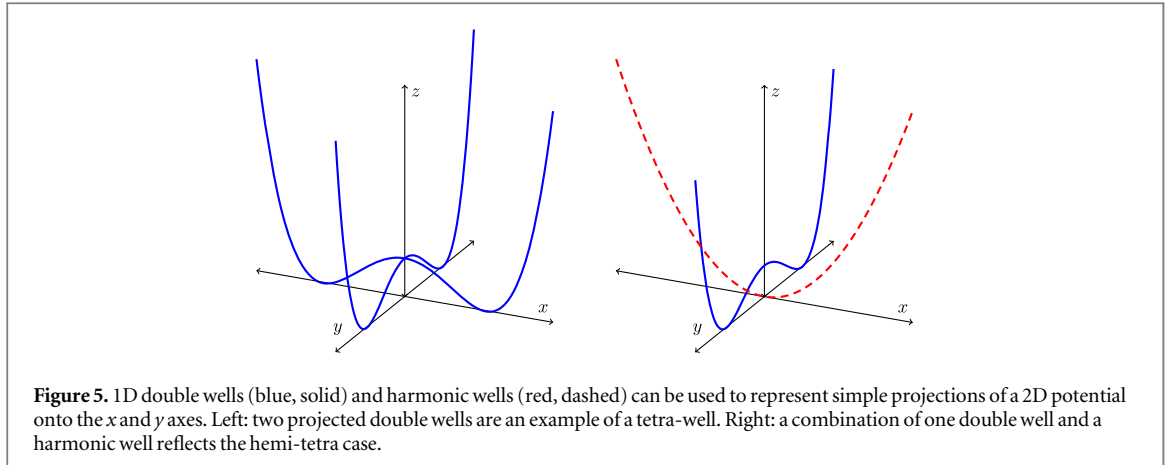
The ξ metric is capable of identifying the tetra- ($\xi = 0$) and hemi-tetra- ($\xi = 1/2$) domains, as well as harmonic ($\xi = 5/4$) and unique ground state (rotationally symmetric, Mexican hat-like) ($\xi = 2$) regimes and finally the location of bifurcations or transitions ($\xi = 1$). Figure 6 shows the corresponding layouts of each interplay. It is worth noting that $\xi = 3/2$ can also be considered harmonic for the lowest three levels.

4.2. Visualizing phase space and identifying TLSs

Using this ξ metric and varying the values of both $|X|$ and $|Y|$ generates figure 7, a phase map of the interplay of low energy states of the oxygen atom confined in 2D by aluminium atoms. The x and y axes show the $|X|$ and $|Y|$ pair separation distances respectively over a range of 1.85–4 Å and the phase colour indicates which ξ region a particular configuration exists in.

Regions that are deemed to be unimportant when searching for TLS behaviour are those where $\xi \geq 1$, as these correspond to eigenspectra which do not possess a (quasi-)doubly degenerate ground state.

As discussed in section 3, in the 1D confinement case, both A and B type defects exist in a hemi-tetra-well ($\xi = 1/2$). This is also the case for the 2D landscape—contour lines corresponding to $E_{01} = \{0.5, 2, 4, 6, 8, 10\}$ GHz (red–yellow) on figure 7 show the configuration properties that result in TLS E_{01} splittings in various qubit



architectures described in section 2. For example: anywhere an orange, 8 GHz line exists on this phase map, the $|X|$, $|Y|$ coordinates of the model generate a cluster configuration that yields the same E_{01} observed in phase qubit experiments [14].

Many of these lines lie completely within a $\xi = 1/2$ (green) region. Consider the contour set on the left of figure 7 where $|X| \approx 1.5 \text{ \AA}$: section 3 states this distance is indicative of an A type defect. The addition of the $|Y|$ aluminium pair does little to perturb the potential at larger distances ($|Y| \gtrsim 3 \text{ \AA}$) and causes only slight deformations at smaller distances ($2 \lesssim |Y| \lesssim 3 \text{ \AA}$). As the phase space is symmetric about $|X| = |Y|$, A type defects exist at the bottom of the plot where $|Y| \approx 1.5 \text{ \AA}$ as well.

B type defects also exist in a $\xi = 1/2$ region, when $|X|$ or $|Y| \approx 2.4 \text{ \AA}$. The orthogonal pair separation distance is at least 1 \AA larger than the defect pair in these configurations and therefore have no bearing on the potential seen by the oxygen. Complications arise when the orthogonal pair is closer and begins to confine the defect. To explain this response, a better understanding of the domains of the map is required.

4.3. Analysis of phase space domains

The case of $\xi = 0$ is particularly interesting in this scenario: a tetra-well region, causing a quad degeneracy in the ground state. In this region, the characteristics of a B type defect are strongly modified. To understand why, we first explain the large rounded $\xi = 0$ domains in the centre of figure 7's phase space.

Tetra-well domains exist when the confinement potential on the oxygen consists of two double wells (see left plot in figure 5). This phenomena emerges when both the defect pair and the confining pair of atoms are close enough to interact. Consider an A type defect with a defect pair in $|X|$ and a confining pair at a constant value of $|Y| = 2.5 \text{ \AA}$. If $|X|$ is varied from an initial value of $1.6\text{--}2 \text{ \AA}$, this extension spans phase space from one point where $E_{01} = 8 \text{ GHz}$ to another. This separation is traced on figure 7 (white dashed-dotted line labelled A), where the defect visibly moves from a hemi-tetra-regime ($\xi = 1/2$) and goes through a transition region before reaching the tetra-well regime ($\xi = 0$). Figure 8 depicts the eigenspectrum of this trace. This is in contrast to larger confining pair values such as $|Y| = 3.6 \text{ \AA}$ (also traced on figure 7: white dashed-dotted line labelled B) where the eigenspectrum is largely unchanged from the 1D case presented in figure 2.

As the $|X|$ separation distance is increased, the effect on E_{01} is negligible on the scale of the higher energy levels (although differs greatly on the TLS splitting energy scale). However, the degenerate pair E_{23} (a degenerate second and third excited state pair) rapidly shifts from a level much higher than ground to quasi-degenerate at ground. Complete quad-degeneracy is not always extant in the tetra-well regime, configurations of $|X|$ and $|Y|$ in these domains usually have two quasi-degenerate pairs which are still observable, akin to the hemi-tetra-

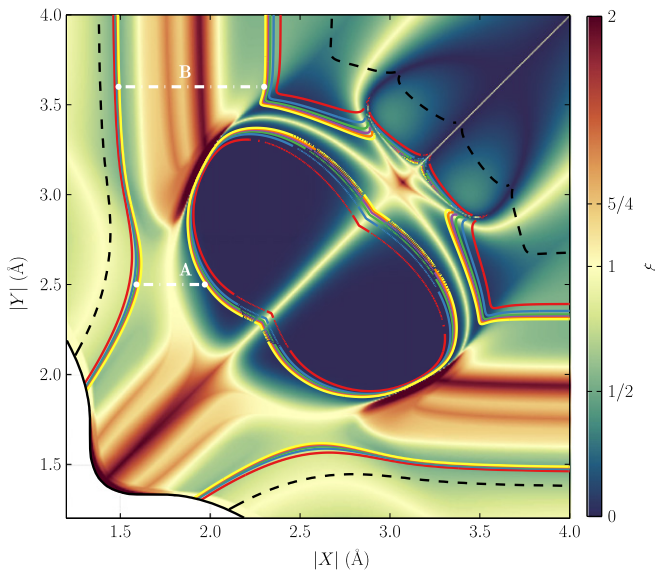


Figure 7. Map of the ξ metric of the delocalized oxygen 2D model. The $|X|$ and $|Y|$ axes represent aluminium pair position separations. Black, dashed contour lines represent a minimum resolvable energy splitting of 10 kHz. The white (blank) section indicates where the aluminium atoms are so close, the oxygen confinement region no longer exists. Overlayed contour lines corresponding to $E_{01} = 0.5\text{--}10$ GHz (red–yellow) are comparable to existing experimental qubit results. Cases where quad-degeneracy exists are denoted as dotted rather than solid contours. Two traces (white, dashed–dotted lines) are also depicted. The first, at $|Y| = 2.5$ Å (labelled A) is plotted in figure 8. In contrast, the trace at $|Y| = 3.6$ Å (labelled B) yields an equivalent eigenspectrum to the 1D case in figure 2.

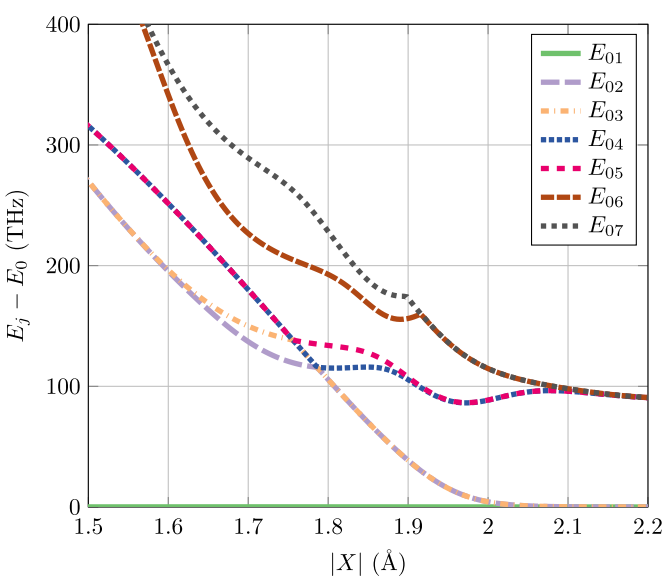


Figure 8. Eigenspectrum of a 2D TLS: an oxygen atom caged with four aluminium atoms. Each excited state has been normalized with the ground state. The confinement pair $|Y|$ is held at a constant distance separation of 2.5 Å and the $|X|$ range shows how higher eigenvalues behave as the confinement atoms force the defect into a tetra-well regime. Figure 7 depicts this data in terms of ξ (white dashed–dotted trace labelled A).

domains, with the difference *between* the pairs approaching the difference *of* the pairs: $E_{01} = E_{23} \approx E_{12}$ ($1.95 \lesssim |X| \lesssim 2$ Å in figure 8 for example). In other words, when the ground to first excited and second to third excited state differences are equal, the first to second excited state difference trends from a much larger value to one effectively equivalent to the aforementioned pairs in this region.

When considering the influence of higher lying excited states, it is important to keep the fundamental energy scales of the problem in mind. In typical qubit experiments, the superconducting properties of the device put a rigorous upper limit on TLS frequencies of interest. At frequencies greater than approximately 100 GHz, there is enough energy to dissociate Cooper-pairs and therefore it can be viewed as an operational upper bound for JJ

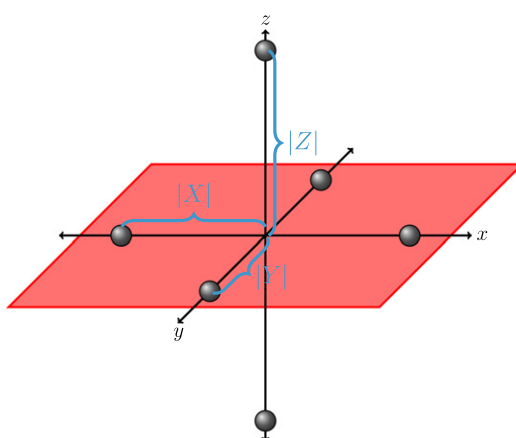


Figure 9. Illustration of an idealized cluster producing a void in 3D. Six cage aluminium atoms (gray) sit in pairs on each cardinal axis, equidistant from the origin. Separation distances $|X|$ and $|Y|$ are labeled for reference (see text). The plane (red) at $z = 0$ is a representation of the 2D delocalization of an oxygen atom.

devices (typical operating frequencies are however device specific, and are much lower in practice). For much of the tetra-well domain $E_{12} \geq 100$ GHz and consequently can effectively be ignored, the system can be considered as a two-level defect even in this quad degeneracy domain.

The B type defects' sudden behaviour change as $|X| \rightarrow |Y|$ is also caused by this response (see figure 7). Confinement pairs start interacting with the defect, causing E_{23} to approach the value of E_{01} (again, $1.95 \lesssim |X| \lesssim 2$ Å in figure 8 depicts this phenomena). The ξ metric does not clearly differentiate between two quasi-degenerate pairs that are marginally separated and two pairs that are actually degenerate.

If however, $E_{12} < 100$ GHz, higher lying energy states must still be considered and the model exhibits true quad degenerate behaviour. Regions in which this occurs are denoted in figure 7 as dotted contours, which over the entirety of phase space are extremely rare—which suggests a reason why quad-level systems are yet to be experimentally observed.

The final domain yet to be discussed on figure 7 is the upper right-hand corner where both $|X|$ and $|Y|$ are large. This region is tetra-well dominated but can be considered as a region where the TLS model breaks down. Each of the four potential minima exist localized about the four confining aluminium atoms and as such should not be considered as TLS candidates.

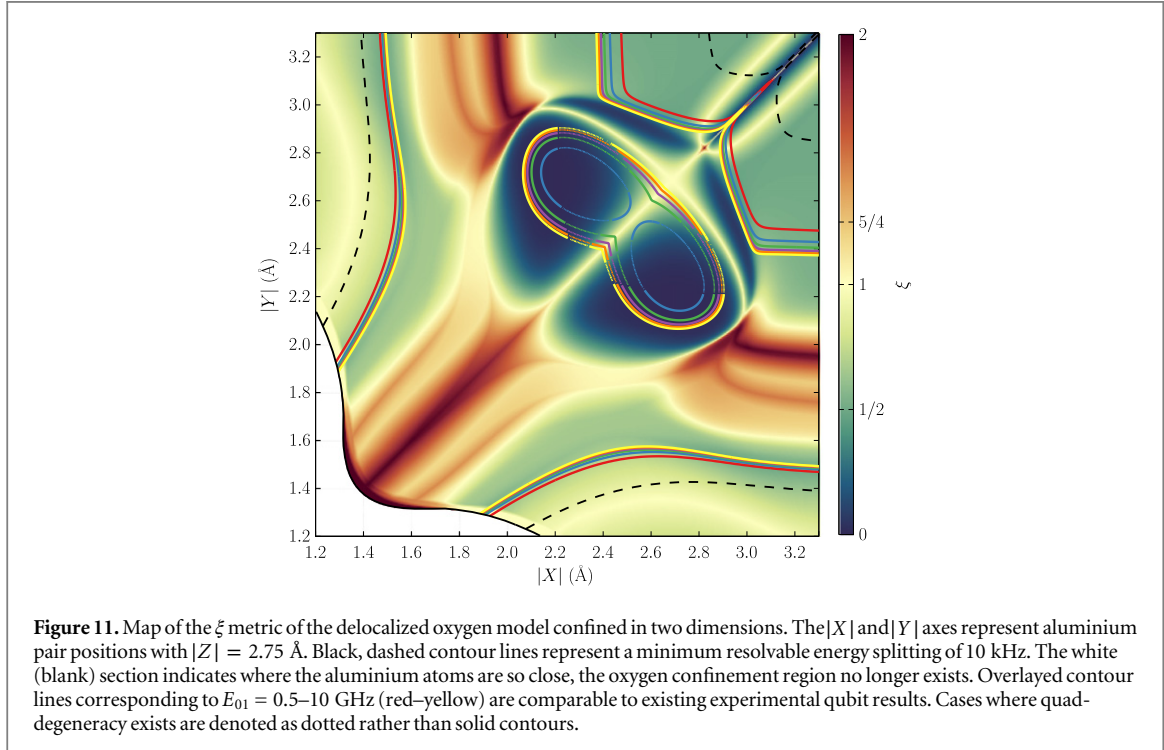
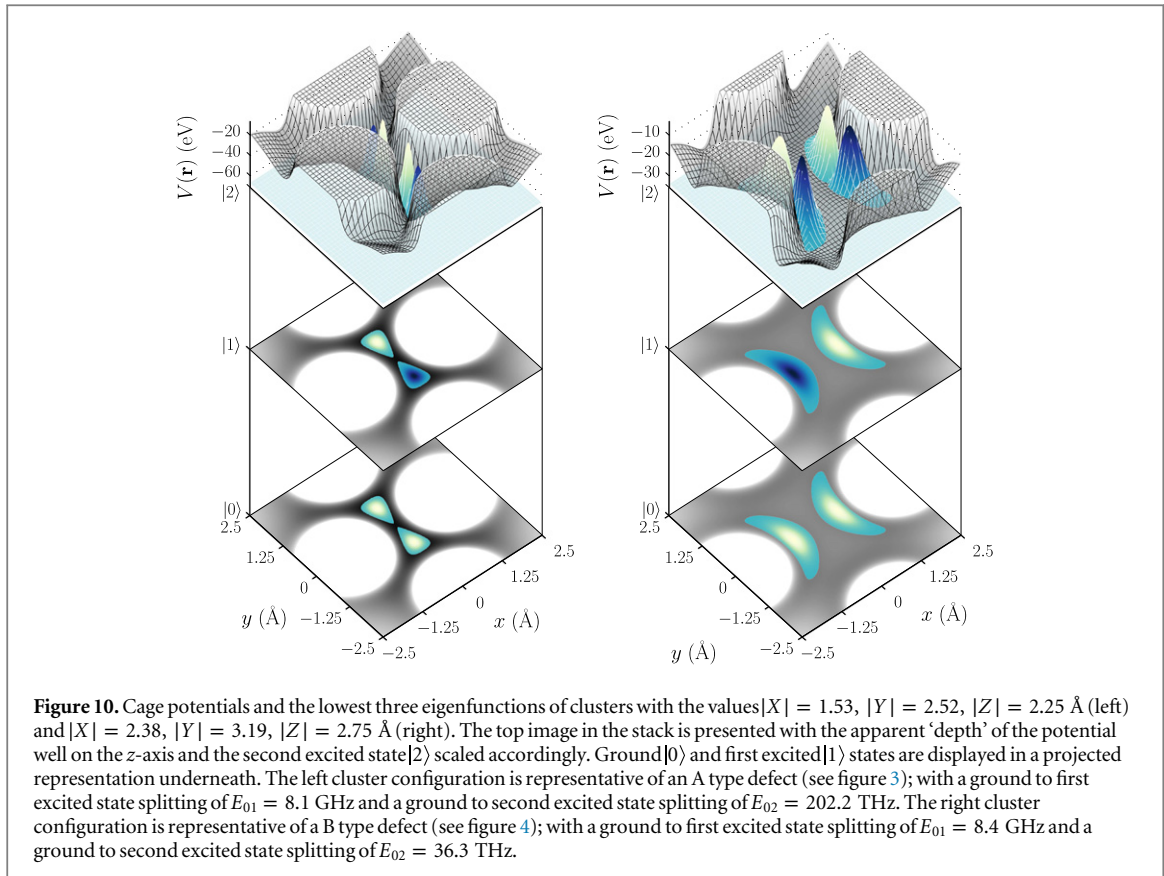
5. TLS defect confined in three dimensions

To understand the properties of a delocalized oxygen, we have considered confining aluminium atoms in both a line and in a plane. In reality, aluminium atoms will surround the oxygen in all three dimensions. Two more confining atoms are therefore added into the system in the z direction labelled as $|Z|$. Interactions with these atoms in the third dimension are now considered, although the model is still 2D (i.e. 2+1D); thus oxygen continues to be confined to the xy plane. An illustration of this cluster configuration is displayed in figure 9 and representations of the cage potential and oxygen wavefunctions are shown in figure 10 for A (left) and B (right) type defects.

The selection of a fixed $|Z|$ distance changes the phase landscape in a manner that can be qualitatively extrapolated between two arbitrary values even a few angstroms apart. Values of $|Z| = 2.75$ Å (figure 11) and $|Z| = 2.25$ Å (figure 12) have been chosen to analyze in detail.

TLS behaviour can be observed on both maps and each value of $|Z|$ has been selected based on model parameters. Oxygen confinement occurs for $|Z|$ values lower than 2.25 Å (i.e. $E_{01} \gg 100$ GHz). $|Z|$ values larger than 2.75 Å show similar phase behaviour to that of figure 7, which is completely unbound in z . Large $|Z|$ separation distances also decrease the validity of the 2+1D model, in addition: the radial distribution analysis in [18] suggests large separation distances for nearest neighbour atoms have a low probability of occurrence.

As the pair separation distance $|Z|$ decreases, the tetra-well ($\xi = 0$) regimes diminish in size and no longer exhibit TLS behaviour. This suggests that quad-degenerate defects, whilst quite rare in phase space already, are extremely rare in reality. For one to exist in a junction, the amorphous layer would have to be disordered in such a way that an oxygen atom's nearest neighbour atom pair exists at a distance greater than ~ 3 Å along one orthogonal basis vector.



Whilst this configuration of six cage aluminium atoms on cardinal axes around a central oxygen is still an idealized system, figure 12 is confined in all three spatial dimensions with pragmatic distances and is therefore considered to be the most ‘realistic’ representation of the TLS phase space for this model published here. TLS candidates lie well within hemi-tetra- ($\xi = 1/2$) domains, are not mired by higher energy level complexities

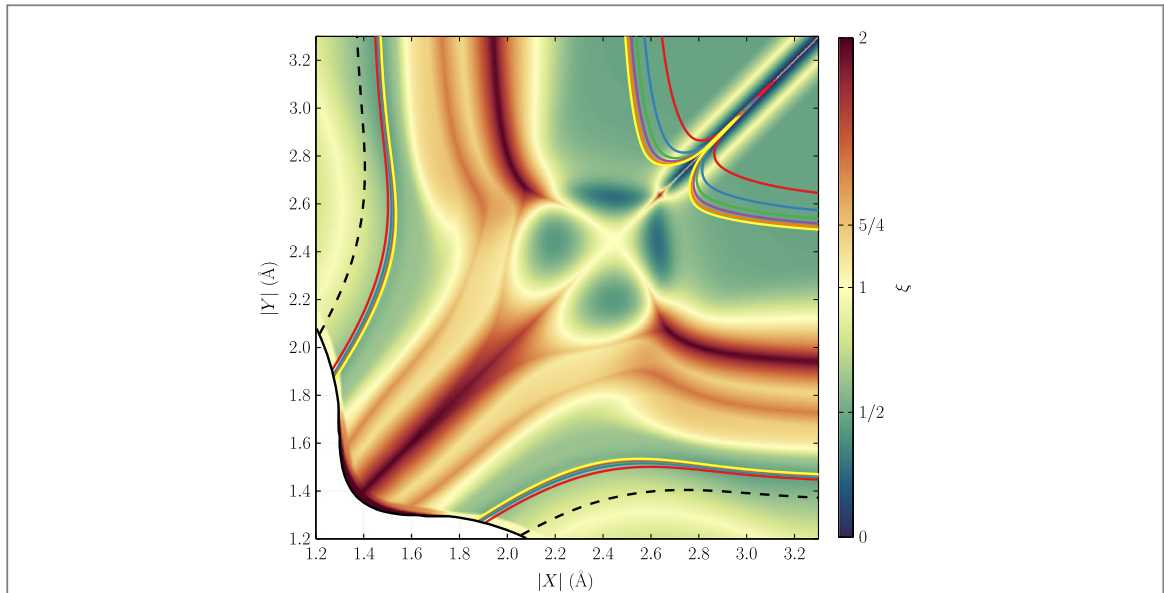


Figure 12. Map of the ξ metric of the delocalized oxygen model confined in two dimensions. The $|X|$ and $|Y|$ axes represent aluminium pair positions with $|Z| = 2.25 \text{ \AA}$. Black, dashed contour lines represent a minimum resolvable energy splitting of 10 kHz. The white (blank) section indicates where the aluminium atoms are so close, the oxygen confinement region no longer exists. Overlayed contour lines corresponding to $E_{01} = 0.5\text{--}10 \text{ GHz}$ (red–yellow) are comparable to existing experimental qubit results.

(i.e. quad-quasi-degeneracies) and can be clearly identified as A type and B type defects separated by an (an) harmonic boundary.

Phase space is also dominated on this map with $\xi = 5/4$ (harmonic) and $\xi = 2$ (unique ground state) domains where the oxygen atom can be considered under the spatial harmonic approximation (i.e. localized). This is significant, as TLS observations in experiments are not statistically dense. We expect few defects in the junction compared to the number of atoms extant.

6. Charge dipoles

As stated in section 2, another important experimentally measurable property of the TLS is its strong electric dipole moment. Using the same $|X|$, $|Y|$ and $|Z|$ parameters from the phase maps in the previous section, the dipole elements in the x direction φ_x , and the y direction φ_y can be calculated via equation (8). Figure 13 shows the same phase space as figure 11, where $|Z| = 2.75 \text{ \AA}$, and figure 14 matches figure 12, where $|Z| = 2.25 \text{ \AA}$. The colourmap for both figures now represent dipole strengths of each cluster configuration rather than energy level splittings (represented through the ξ metric). These computed dipole moments correspond well to observed values, assuming $\mathcal{O}(\text{nm})$ junction widths [9, 14].

The dipole moments are presented as $(|\varphi_y| - |\varphi_x|)/e$ rather than separate plots because the dipole elements are discontinuous at the bifurcation points (i.e. when $|\varphi_x| > 0$, $|\varphi_y| = 0$ and vice versa). Comparing these plots to the phase maps in section 5, it is apparent that only the tetra- and hemi-tetra- domains ($\xi < 1$) exhibit a dipole response—which is appropriate for our model as E_{01} splittings representative of a TLS only appear in these regions. Localized oxygen atoms ($\xi > 1$) are also expected to not elicit dipole behaviour.

With this information, the domain boundaries and bifurcations on each phase map can now be fully explained. Two variables alter the landscape: dipole and potential. Clusters with tight z confinement (those without tetra-well regions such as $|Z| = 2.25 \text{ \AA}$) have four unique regions where a TLS may reside. The dipole direction dominates two of these domains: an A type region when the confining pair is collinear to the dipole, and a B type region when the confining pair is perpendicular. A symmetry bifurcation (at $|X| = |Y|$) separates the dipole domains into four regions which can therefore be clearly identified in terms of dipole moment ($|\varphi_x|$ or $|\varphi_y|$) and defect type (A or B).

Clusters without as much z confinement (such as $|Z| = 2.75 \text{ \AA}$) exhibit tetra-well behaviour: generating two additional regions. Tetra-well domains, as discussed in section 4.3, are caused when the confining pair of aluminium atoms start interacting with the defect pair (and hence the oxygen as well). If we consider the A type, $|\varphi_y|$ domain in figure 13, it is clear that the dominant dipole direction remains constant as $|X|$ separation is increased and the tetra-well domain is entered. The same $|X|$, $|Y|$ parameters on figure 14 cross a bifurcation line, changing dipole direction and the model indicates B type defect properties. Increased confinement in z

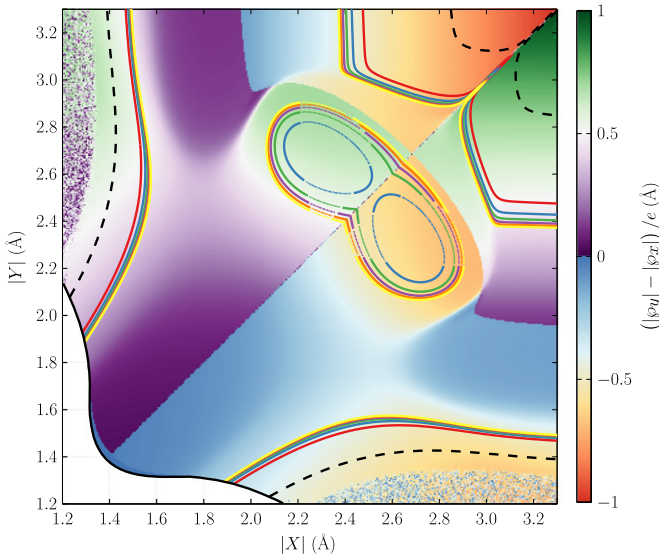


Figure 13. The difference between the absolute dipole moment (in x - and y -directions) over the same range for $|Z| = 2.75 \text{ \AA}$. We see either $|\varphi_x|$ (red) or $|\varphi_y|$ (green) dominated behaviour in the tetra and hemi-tetra domains but none in other regions.

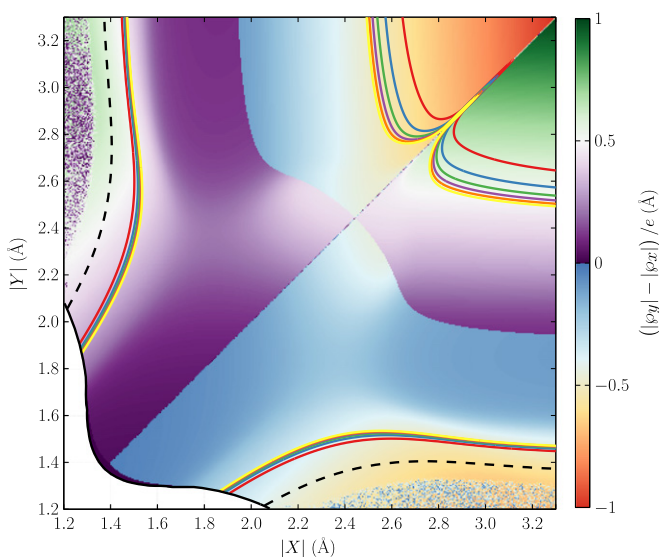


Figure 14. The difference between the absolute dipole moment (in x - and y -directions) over the same range for $|Z| = 2.25 \text{ \AA}$. We see either $|\varphi_x|$ (red) or $|\varphi_y|$ (green) dominated behaviour in the tetra and hemi-tetra domains but none in other regions.

induces a deeper potential well in the xy plane and removes any major landscape changing contributions from the confining atom pair—effectively reducing the model back to a 1D description. A cluster with a comparatively shallow potential that generates tetra-well domains does so when conditions are advantageous for an A type confinement pair to become a B type defect pair (a dipole direction change is not required for this to occur). A trace like the $|Y| = 2.5 \text{ \AA}$ (labelled A) on figure 7 (and an associated eigenspectrum response similar to figure 8) is an example of this behaviour. If we do not consider the small portion of quad-degenerate defects in this domain; the measurable properties (i.e. E_{01} and dipole strength) tetra-well, B type, $|\varphi_y|$ TLSs are identical to B type, $|\varphi_y|$ TLSs that reside in a hemi-tetra-well domain.

7. Qubit coupling

To compare our TLS model directly to experiments, we assume that our JJ lies within a phase qubit, although the model applies equally for any device comprised of amorphous junctions. The measurable signal of a TLS in a

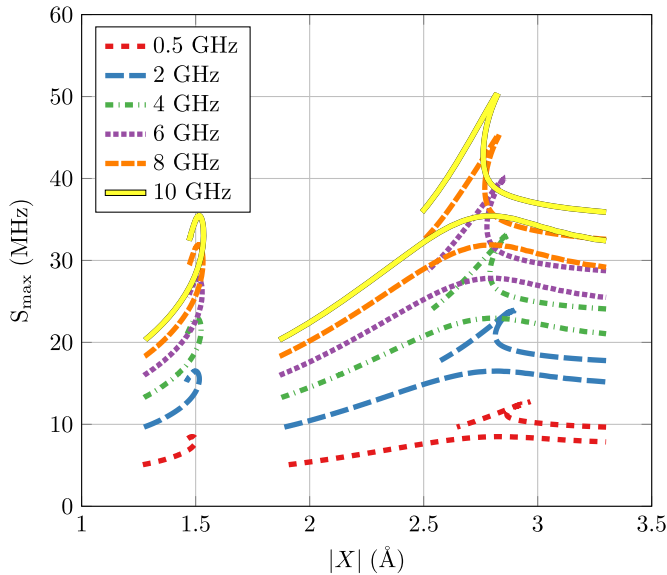


Figure 15. Coupling strength to a fictitious phase-qubit S_{\max} as a function of $|X|$ in the domains where both dipoles $|\varphi_{x,y}|$ are dominant (see (10) for a set of constant E_{01} splitting frequencies) and $|Z| = 2.25 \text{ \AA}$.

phase qubit is the resonance of the TLS and qubit splitting energy, E_{01} , with the qubit–TLS coupling. For the phase qubit [9], the qubit–TLS coupling S_{\max} is a function of E_{01} and φ [41], the effective dipole moment due to an electric field applied in the direction of delocalization

$$S_{\max} = 2 \frac{\varphi}{w} \sqrt{\frac{e^2}{2C} E_{01}}. \quad (10)$$

Throughout this discussion we assume a junction width $w = 2 \text{ nm}$ and capacitance $C = 850 \text{ fF}$.

The dipole magnitudes in figures 13 and 14 are calculated against the electron charge for simplicity, although as we are discussing an oxygen atom, the dipole elements may in fact be larger. Using our JJ DFT models [18] we partition the charge density associated with atoms across the lattice into Bader volumes [42]. The charge enclosed within each Bader volume is a good approximation to the total electronic charge of an atom. An average value of $1.395 \pm 0.006 e$ is found for oxygen atoms in a junction comprised of $\text{AlO}_{0.5}$ at a density of 0.8 times that of corundum (a common, low temperature and pressure phase of Al_2O_3). We can use this value such that

$$\widetilde{\varphi}_x = 1.4e\varphi_x \quad (11)$$

(for a dipole in the x direction) to gain a better estimate of S_{\max} .

In figure 15 we plot contour lines representing constant values of E_{01} which correspond to the purview of experimentally observed qubit resonant frequencies for constant values of $|Z| = 2.25 \text{ \AA}$. The S_{\max} (10) response to these frequencies is plotted as a function of $|X|$, in which we see maximum coupling strengths which correspond exceptionally well with experimental observations [5, 6, 14]. The most comprehensive of these studies [5] measures S_{\max} values of 3–45 MHz, assuming a 1 Å dipole moment.

Whilst the S_{\max} response is neither smooth nor singular over the phase space investigated, the value range is surprisingly small. Figure 16 shows the range of S_{\max} couplings for all $E_{01} = 8 \text{ GHz}$ configurations calculated with confinements in $|Z|$ from 2.25 Å to unbound and $|X|$ (hence $|Y|$ as well from symmetry arguments) from 1.2 to 4 Å. The entire range of S_{\max} values is only 60 MHz wide, which suggests an explanation as to why large couplings (of order 500 MHz for example) have not been seen experimentally.

8. Strain response

Unusually long coherence times of strongly coupled defects are a key observation of TLS–qubit experiments [4, 43]. As our model assumes a charge-neutral defect, coherence time is linked to the dipole element (for charge noise) and the strain response (for phonons). Mechanical deformation of a phase-qubit has recently been observed directly [44], which we can mimic in our 2D model by introducing a series of deformations onto the cluster, and subsequently measure the E_{01} response.

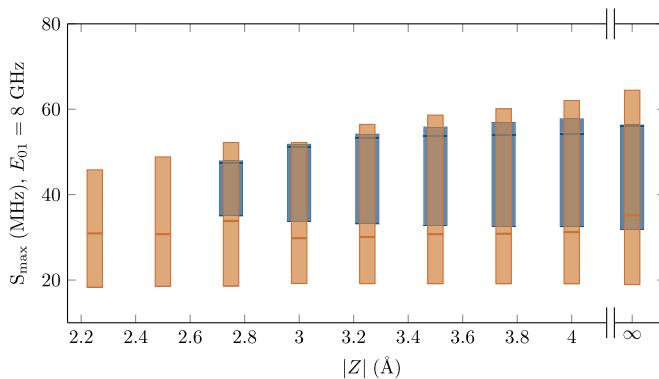


Figure 16. S_{\max} response range for a constant E_{01} splitting frequency of 8 GHz as a function of $|Z|$ separation. Each box on the figure represents the minimum to maximum S_{\max} values in both $|\varphi_x|$ and $|\varphi_y|$ dominant domains over the phase space of $|X|$ distance separations. The box at $|Z| = 2.25 \text{ \AA}$ represents all $E_{01} = 8 \text{ GHz}$ values on figure 15 for example. Median values are plotted as solid lines inside each box. Orange (thin) boxes represent quasi-degenerate regions and blue (thick) boxes indicate quad-degenerate regions.

Whilst many deformation types were tested [18], only two types (depicted in figure 17(a) show an active response over a length change (ΔL) of 1 pm. Four clusters are chosen that lie on the 8 GHz contour when $|Z| = 2.25 \text{ \AA}$, indicated as (b), (c), (d) and (e) in figure 17(a). As can be seen in figure 14, each of these cases are within a $|\varphi_x|$ dominant domain.

The investigation in [18] focused on $|X|$ translation due to its large, hyperbolic response—which is also seen in experiments [44]. The cluster configuration considered had a $|Z|$ confinement of 2.5 \AA and the same $|X|, |Y|$ separations as published here; thus it is not surprising that $|X|$ translation yields an E_{01} response is of $\sim 10^4 \text{ GHz}$ for $|Z| = 2.25 \text{ \AA}$ also. Therefore, translation of $|X|$ has not been included in figure 17 or the following discussion.

Clusters (b) and (c) are both identified as A type defects and are relatively insensitive to $|X|$ dilation and $|Y|$ translation. Dilation of $|Y|$ for these defects is a different way of saying ‘extending the defect pair separation’—which has been described in the above sections. The intensity of the response however is noticeably larger as the confinement distance ($|X|$) is increased.

B type defects, labelled (d) and (e), respond discordantly depending on their configuration. Dilation in $|Y|$, whilst a sizable strain source for A type configurations, initiates no response from the (e) configuration at all. B type defects located at this position in phase space have their defect pair in $|X|$, and point (e) specifically is confined with $|Y| = 3.1 \text{ \AA}$. As discussed in the sections above, this separation distance is close to being practically unbound. Point (d) on the other hand has a tighter separation distance and begins to confine the system. Dilation in $|X|$ responds in the opposite manner effectively: expanding defect separation distance whilst keeping the confinement distance static ultimately confines the wavefunction. The final response that the B type defects respond to is $|Y|$ translation. As point (e) is essentially unbound in $|Y|$ we do not expect any response from a strain of this magnitude. Point (d) on the other hand is interacting with its tighter confinement distance, with the TLS dipole collinear to the $|X|$ direction. Translation of $|Y|$ forces local minima of the potential landscape from points on the x axis to locations off axis, yet still within the minima rings about the aluminium atoms. In other words, the wavefunction is slightly rotated around the defect axis.

9. Conclusions and outlook

Even with the extreme idealization of this model, it allows the prediction of experimentally measured properties of strongly coupled TLSs with atomic positions as the only input parameters and therefore shows as a proof of concept that these defects can arise in AlO_x without any alien species present.

Our model shows that even when only considering delocalization in 2D, a range of different behaviour can be seen. The existence of effective two-state systems can come about through different potential shapes, which in turn arise due to various atomic position configurations. To understand these different configurations, we consider both the symmetries of the eigenspectrum and the effective charge dipole of the defect.

We find that TLSs with equivalent properties to those seen in experiments can be formed from atomic configurations which are entirely consistent with the material properties of amorphous aluminium oxide barriers. Most interestingly we find that the expected qubit–TLS coupling strength and the TLS strain response correspond very well to that observed experimentally.

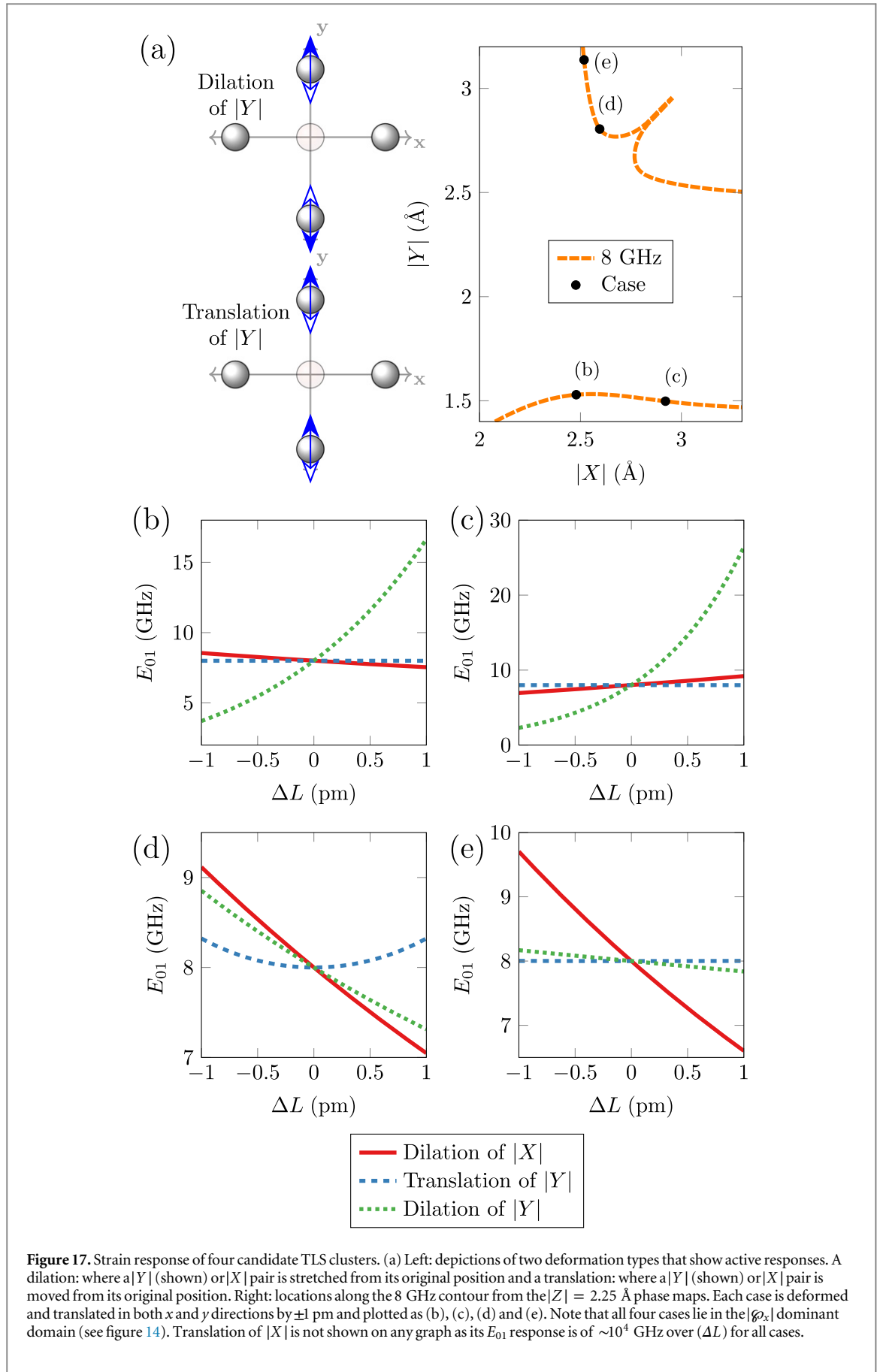


Figure 17. Strain response of four candidate TLS clusters. (a) Left: depictions of two deformation types that show active responses. A dilation: where a $|Y|$ (shown) or $|X|$ pair is stretched from its original position and a translation: where a $|Y|$ (shown) or $|X|$ pair is moved from its original position. Right: locations along the 8 GHz contour from the $|Z| = 2.25 \text{ \AA}$ phase maps. Each case is deformed and translated in both x and y directions by $\pm 1 \text{ pm}$ and plotted as (b), (c), (d) and (e). Note that all four cases lie in the $|\varphi_x|$ dominant domain (see figure 14). Translation of $|X|$ is not shown on any graph as its E_{01} response is of $\sim 10^4 \text{ GHz}$ over (ΔL) for all cases.

A complication that occurs with phenomenological models that attempt to describe TLS behaviour is their free parameter count is high enough to describe all facets of the observed experimental parameters without being distinguishable from other, non-complimentary models [14]. Whilst this delocalized oxygen model only uses one type of parameter as input (atomic positions), it still requires an x , y , z coordinate set for up to six cage atoms. More sophisticated modelling techniques such as molecular mechanics and density functional methods can be then used to obtain more realistic values for the atomic positions [18]. Microscopic models of this type will guide future fabrication and design of superconducting circuits, leading to lower levels of noise and greater control over their quantum properties.

Acknowledgments

This research was supported under the Australian Research Council's Discovery Projects funding scheme (project number DP140100375). Computational resources were provided at the NCI National Facility systems at the Australian National University through the National Computational Merit Allocation Scheme supported by the Australian Government.

References

- [1] Dutta P and Horn P 1981 Low-frequency fluctuations in solids: 1f noise *Rev. Mod. Phys.* **53** 497–516
- [2] Shnirman A, Schön G, Martin I and Makhlin Y 2005 Low- and high-frequency noise from coherent two-level systems *Phys. Rev. Lett.* **94** 127002
- [3] Simmonds R, Lang K, Hite D, Nam S, Pappas D and Martinis J 2004 Decoherence in Josephson phase qubits from junction resonators *Phys. Rev. Lett.* **93** 077003
- [4] Neeley M, Ansmann M, Bialczak R C, Hofheinz M, Katz N, Lucero E, O'Connell A, Wang H, Cleland A N and Martinis J M 2008 Process tomography of quantum memory in a Josephson-phase qubit coupled to a two-level state *Nat. Phys.* **4** 523–6
- [5] Shalibo Y, Rofe Y, Shwa D, Zeides F, Neeley M, Martinis J M and Katz N 2010 Lifetime and coherence of two-level defects in a Josephson junction *Phys. Rev. Lett.* **105** 177001
- [6] Lupacu A, Bertet P, Driessens E F C, Harmans C J P M and Mooij J E 2009 One- and two-photon spectroscopy of a flux qubit coupled to a microscopic defect *Phys. Rev. B* **80** 172506
- [7] Lisenfeld J, Müller C, Cole J H, Bushev P, Lukashenko A, Shnirman A and Ustinov A V 2010 Measuring the temperature dependence of individual two-level systems by direct coherent control *Phys. Rev. Lett.* **105** 230504
- [8] Gunnarsson D, Pirkkalainen J-M, Li J, Paraoanu G S, Hakonen P, Sillanpää M and Prunnila M 2013 Dielectric losses in multi-layer Josephson junction qubits *Supercond. Sci. Technol.* **26** 085010
- [9] Martinis J et al 2005 Decoherence in Josephson qubits from dielectric loss *Phys. Rev. Lett.* **95** 210503
- [10] de Sousa R, Whaley K, Hecht T, Delft J v and Wilhelm F 2009 Microscopic model of critical current noise in Josephson-junction qubits: subgap resonances and Andreev bound states *Phys. Rev. B* **80** 094515
- [11] Sendelbach S, Hover D, Kittel A, Mück M, Martinis J and McDermott R 2008 Magnetism in SQUIDs at millikelvin temperatures *Phys. Rev. Lett.* **100** 227006
- [12] Faoro L and Ioffe L 2007 Microscopic origin of critical current fluctuations in large, small, and ultra-small area Josephson junctions *Phys. Rev. B* **75** 132505
- [13] Ku L-C and Yu C 2005 Decoherence of a Josephson qubit due to coupling to two-level systems *Phys. Rev. B* **72** 024526
- [14] Cole J H, Müller C, Bushev P, Grabovskij G J, Lisenfeld J, Lukashenko A, Ustinov A V and Shnirman A 2010 Quantitative evaluation of defect-models in superconducting phase qubits *Appl. Phys. Lett.* **97** 3
- [15] Agarwal K, Martin I, Lukin M and Demler E 2013 Polaronic model of two-level systems in amorphous solids *Phys. Rev. B* **87** 144201
- [16] Lee D, DuBois J and Lordi V 2014 Identification of the local sources of paramagnetic noise in superconducting qubit devices fabricated on α -Al₂O₃ substrates using density-functional calculations *Phys. Rev. Lett.* **112** 017001
- [17] Anderson P W, Halperin B I and Varma C M 1972 Anomalous low-temperature thermal properties of glasses and spin glasses *Phil. Mag.* **25** 1–9
- [18] DuBois T C, Per M C, Russo S P and Cole J H 2013 Delocalized oxygen as the origin of two-level defects in Josephson junctions *Phys. Rev. Lett.* **110** 077002
- [19] Choi S, Lee D-H, Louie S and Clarke J 2009 Localization of metal-induced gap states at the metal-insulator interface: origin of flux noise in SQUIDS and superconducting qubits *Phys. Rev. Lett.* **103** 197001
- [20] Jameson J R, Ngo D, Benko C, McVittie J P, Nishi Y and Young B a 2011 Dielectric relaxation study of hydrogen exposure as a source of two-level systems in Al₂O₃ *J. Non-Cryst. Solids* **357** 2148–51
- [21] Holder A M, Osborn K D, Lobb C J and Musgrave C B 2013 Bulk and surface tunneling hydrogen defects in alumina *Phys. Rev. Lett.* **111** 065901
- [22] Vion D, Aassime A, Cottet A, Joyez P, Pothier H, Urbina C, Esteve D and Devoret M H 2002 Manipulating the quantum state of an electrical circuit *Science* **296** 886–9
- [23] Koch J, Yu T, Gambetta J, Houck A, Schuster D, Majer J, Blais A, Devoret M, Girvin S and Schoelkopf R 2007 Charge-insensitive qubit design derived from the Cooper pair box *Phys. Rev. A* **76** 042319
- [24] Schreier J et al 2008 Suppressing charge noise decoherence in superconducting charge qubits *Phys. Rev. B* **77** 180502
- [25] Houck A et al 2008 Controlling the spontaneous emission of a superconducting transmon qubit *Phys. Rev. Lett.* **101** 080502
- [26] Artacho E, Lizón-Nordström A and Ynduráin F 1995 Geometry and quantum delocalization of interstitial oxygen in silicon *Phys. Rev. B* **51** 7862–5
- [27] Zachariases W H 1932 The atomic arrangement in glass *J. Am. Chem. Soc.* **54** 3841–51
- [28] Enss C and Hunklinger S 2005 *Low-Temperature Physics* (Berlin: Springer)
- [29] Buchenau U, Nücker N and Dianoux A 1984 Neutron scattering study of the low-frequency vibrations in vitreous silica *Phys. Rev. Lett.* **53** 2316–9

- [30] Heuer A 1998 Microscopic view of the low-temperature anomalies in glasses *Tunneling Systems in Amorphous and Crystalline Solids* P Esquinazi (Berlin: Springer) ch 8
- [31] Trachenko K O, Dove M T, Harris M J and Heine V 2000 Dynamics of silica glass: two-level tunnelling states and low-energy floppy modes *J. Phys.: Condens. Matter* **12** 8041–64
- [32] Reinisch J and Heuer A 2005 What is moving in silica at 1 K? A computer study of the low-temperature anomalies *Phys. Rev. Lett.* **95** 155502
- [33] Schwarz M J, Goetz J, Jiang Z, Niemczyk T, Deppe F, Marx A and Gross R 2013 Gradiometric flux qubits with a tunable gap *New J. Phys.* **15** 045001
- [34] Streitz F and Ram J 1994 Electrostatic potentials for metal-oxide surfaces and interfaces *Phys. Rev. B* **50** 11996–2003
- [35] Catlow C, James R, Mackrodt W and Stewart R 1982 Defect energetics in α -Al₂O₃ and rutile TiO₂ *Phys. Rev. B* **25** 1006–26
- [36] Dienes G, Welch D, Fischer C, Hatcher R, Lazareth O and Samberg M 1975 Shell-model calculation of some point-defect properties in α -Al₂O₃ *Phys. Rev. B* **11** 3060–70
- [37] Rappe A K and Goddard William A 1991 Charge equilibration for molecular dynamics simulations *J. Phys. Chem.* **95** 3358–63
- [38] Zhou X, Wadley H, Filhol J-S and Neurock M 2004 Modified charge transfer embedded atom method potential for metal/metal oxide systems *Phys. Rev. B* **69** 035402
- [39] Gale J D and Rohl A L 2003 The general utility lattice program (GULP) *Mol. Simul.* **29** 291–341
- [40] Mathews J H and Fink K D 2004 *Numerical Methods Using Matlab* 4th edn (Upper Saddle River, NJ: Pearson)
- [41] Kofman A, Zhang Q, Martinis J and Korotkov A 2007 Theoretical analysis of measurement crosstalk for coupled Josephson phase qubits *Phys. Rev. B* **75** 014524
- [42] Tang W, Sanville E and Henkelman G 2009 A grid-based Bader analysis algorithm without lattice bias *J. Phys.: Condens. Matter* **21** 084204
- [43] Lisenfeld J, Müller C, Cole J H, Bushev P, Lukashenko A, Shnirman A and Ustinov A V 2010 Rabi spectroscopy of a qubit-fluctuator system *Phys. Rev. B* **81** 100511
- [44] Grabovskij G J, Peichl T, Lisenfeld J, Weiss G and Ustinov A V 2012 Strain tuning of individual atomic tunneling systems detected by a superconducting qubit *Science* **338** 232–4